IPEM
Institute of Physics and
Engineering in Medicine

PAPER

A dynamic-static combination model based on radiomics features for prostate cancer using multiparametric MRI

View the article online for updates and enhancements.

Physics in Medicine & Biology

IPEM
Institute of Physics and
Engineering in Medicine

PAPER

CrossMark

A dynamic-static combination model based on radiomics features for prostate cancer using multiparametric MRI

Shuqin Li[1], Tingting Zheng[1], Zhou Fan[1], Hui Qu[1], Jianfeng Wang[2], Jianbin Bi[2], Qingjie Lv[3], Gejun Zhang[2,*], Xiaoyu Cui[1,4,*] and Yue Zhao[1,5,*]

1   College of Medicine and Biological Information Engineering, Northeastern University, Shenyang, 110169, People's Republic of China
2   Department of Urology Surgery, The First Hospital of China Medical University, No.155 Nanjing North Street, Heping District, Shenyang, People's Republic of China
3   Department of Pathology, Shengjing Hospital of China Medical University, Sanhao Street 36, Shenyang, 110001, People's Republic of China
4   Key Laboratory of Intelligent Computing in Medical Image, Ministry of Education, Northeastern University, Shenyang, 110169, People's Republic of China
5   National and Local Joint Engineering Research Center of Immunodermatological Theranostics, No.155 Nanjing Bei Street, Heping District, Shenyang, 110001, People's Republic of China
*   Authors to whom any correspondence should be addressed.

E-mail: 13897909605@163.com, cuixy@bmie.neu.edu.cn and zhaoyue@bmie.neu.edu.cn

Abstract

Objective. To propose a new dynamic multiparametric magnetic resonance imaging (mpMRI) radiomics method for the detection of prostate cancer (PCa), and establish a combined model using dynamic and static radiomics features based on this method. *Approach*. A total of 166 patients (82 PCa patients and 84 non-PCa patients) were enrolled in the study, and 31 872 mpMRI images were performed in a radiomics workflow. The whole prostate segmentation and traditional static radiomics features extraction were performed on intravoxel incoherent motion diffusion-weighted imaging (IVIM-DWI, *b* value of 10, 50, 100, 150, 200, 400, 600, 800, 1000, 1500 s mm^{-2} respectively), apparent diffusion coefficient (ADC), and T2-weighted imaging (T2WI) sequences respectively. Through the building of each *b*-value DWI model and the analysis of the static key radiomics features, three types of dynamic features called standard discrete (SD), parameter (*P*) and relative change rate (RCR) were constructed. And the b-value parameters used to construct dynamic features were divided into three groups ('Df_', 'Db_' and 'Da_'): the front part (10–200 s mm^{-2}), the back part (400–1500 s mm^{-2}), and all (10–1500 s mm^{-2}) of the *b*-values set, respectively. Afterwards, the dynamic mpMRI model and combined model construction were constructed, and the PCa discrimination performance of each model was evaluated. *Main results.* The models based on dynamic features showed good potential for PCa identification. Where, the results of Db_SD, Da_P and Db_P models were encouraging (test cohort AUCs: 90.78%, 87.60%, 86.3%), which was better than the commonly used ADC model (AUC of ADC was 75.48%). Among the combined models, the models using static features of T2WI and dynamic features performed the best. The AUC of Db_SD + T2WI, Db_P + T2WI and Db_RCR + T2WI model was 92.90%, 91.29% and 81.46%. *Significance.* The dynamic-static combination model based on dynamic mpMRI radiomics method has a good effect on the identification of PCa. This method has broad application prospects in PCa individual diagnosis management.

Introduction

Globally, prostate cancer (PCa) is the second most common and fifth deadliest cancer in men (Sung *et al* 2021). Early and accurate diagnosis of prostate cancer is very important for improving the survival rate and reducing treatment costs. Multiparametric magnetic resonance imaging (mpMRI) has been proven to be a non-invasive

and effective method for detecting prostate cancer, which can provide a qualitative evaluation of medical imaging and reduce the number of unnecessary biopsies by guiding more accurate sampling (Ahmed *et al* 2017, Fulgham *et al* 2017, Kasivisvanathan *et al* 2018, Mottet *et al* 2022). mpMRI consists of morphological sequence and functional information sequence imaging, and standardized prostate MRI is acquired, interpreted and reported using Prostate Imaging Reporting and Data System (PI-RADS v2.1), focusing on the imaging characteristics of T2-weighted imaging (T2WI), diffusion-weighted imaging (DWI) and dynamic contrast-enhanced imaging (DCE) (Thompson *et al* 2016, Weinreb *et al* 2016, Turkbey *et al* 2019). However, PI-RADS based diagnosis is subjective and relies heavily on the clinical experience of the radiologist, and its accuracy and reproducibility are easily affected by the subjective impression of the observer (Hofbauer *et al* 2018, Kasivisvanathan *et al* 2018, Mottet *et al* 2022).

Radiomics can extract quantitative features from medical images and convert medical images into high-dimensional data that can be mined (Lambin *et al* 2012, Limkin *et al* 2017, Liu *et al* 2019), providing more opportunities for quantitative and objective evaluation of PCa medical images, thus improving the preoperative diagnostic performance of PCa (Cuocolo *et al* 2021, Leech *et al* 2021, Yi *et al* 2022). However, previous studies on prostate imaging are almost all based on traditional static radiomics features, ignoring the changes and differences of radiomics features at different times or under different specific external conditions, which are likely to indirectly reflect the specific metabolic differences of the lesion tissues (Russo *et al* 2012). For example, Sushentsev *et al* (2022) predicted the progression of PCa by analyzing changes in radiomics features at any two time points (i.e. delta-radiomics features) of the same active surveillance patient and verified that the model performed comparable to the PRECISE scores applied by expert readers. Recently, Qu *et al* (2022) constructed a new dynamic feature to describe the changes of static features of the same or different imaging examinations over time, and proposed a dynamic radiomics methodology that is superior to static features analysis in diagnosis and prognosis of some of tumors. Therefore, the study of dynamic features based on the changes and differences of traditional static radiomics features may provide a way to obtain dynamic information. Dynamic features can also assess the heterogeneity of the tumor and its overall microenvironment characteristics as well as traditional static radiomics features, with even better predictive performance (Fave *et al* 2017, Qu *et al* 2022).

Based on the traditional DWI, the intravoxel incoherent motion diffusion-weighted imaging (IVIM-DWI) technology adopts multiple diffusion gradient factors (*b*-values) for scanning and imaging, which is an information-rich 'function' sequence used to detect tissue functions (Bihan *et al* 1988). IVIM-DWI can characterize tissue microstructure and microcirculation by combining diffusion imaging at low and high *b*-value, thus providing more information for tissue characterization in the prostate gland. With the rapid development of MRI technology, the clinical application of IVIM-DWI has been greatly promoted, and a large number of studies have shown the strong potential of IVIM-DWI in the diagnosis and treatment effect monitoring of prostate cancer (Iima and Le Bihan 2016, Sauer *et al* 2018, Kooreman *et al* 2021). However, no consensus has been reached on the quantity and size of b-value used in prostate imaging acquisition, whether it is clinically commonly used DWI or advanced IVIM-DWI (Iima and Le Bihan 2016). The dynamic features constructed in this study may be able to integrate the image characteristics of IVIM-DWI or DWI at multiple b-values and contribute to image analysis.

Therefore, our study aims to establish a dynamic mpMRI radiomics method, and to evaluate a dynamic-static combined PCa prediction model developed by this method.

Materials and methods

Patient population

The study was approved by the local institutional review board, and written informed consent was waived. We retrospectively screened patients who underwent prostate MRI at the First Affiliated Hospital of China Medical University Hospital between July 2019 and August 2021. Inclusion criteria were as follows: (a) pathological results were complete; (b) MRI examination contained T2WI, multiple *b*-values IVIM-DWI and ADC maps; (c) serum prostate-specific antigen (PSA) levels were measured within 8 weeks before MRI examination; (d) prostate biopsy was performed within 4 weeks of MRI examination. Exclusion criteria were as follows: (a) clinical data were incomplete; (b) IVIM-DWI sequence did not completely contain images at *b*-values of 10, 50, 100, 150, 200, 400, 600, 800, 1000, 1500 s mm^{-2}; (c) biopsy was performed within 6 months prior to MRI examination; (d) medical treatment, such as radiation, hormone therapy, or surgery, prior to the MRI examination; (e) prostate was invaded by other tumors.

The final study population consisted of 166 patients, and biopsy results included 82 PCa patients and 84 benign prostatic disease patients. The enrolled patients were randomly assigned to either the training cohort ($n = 116$) or the test cohort ($n = 50$) in a 7:3 ratio, with one label per patient. The overall research workflow is shown in figure 1.
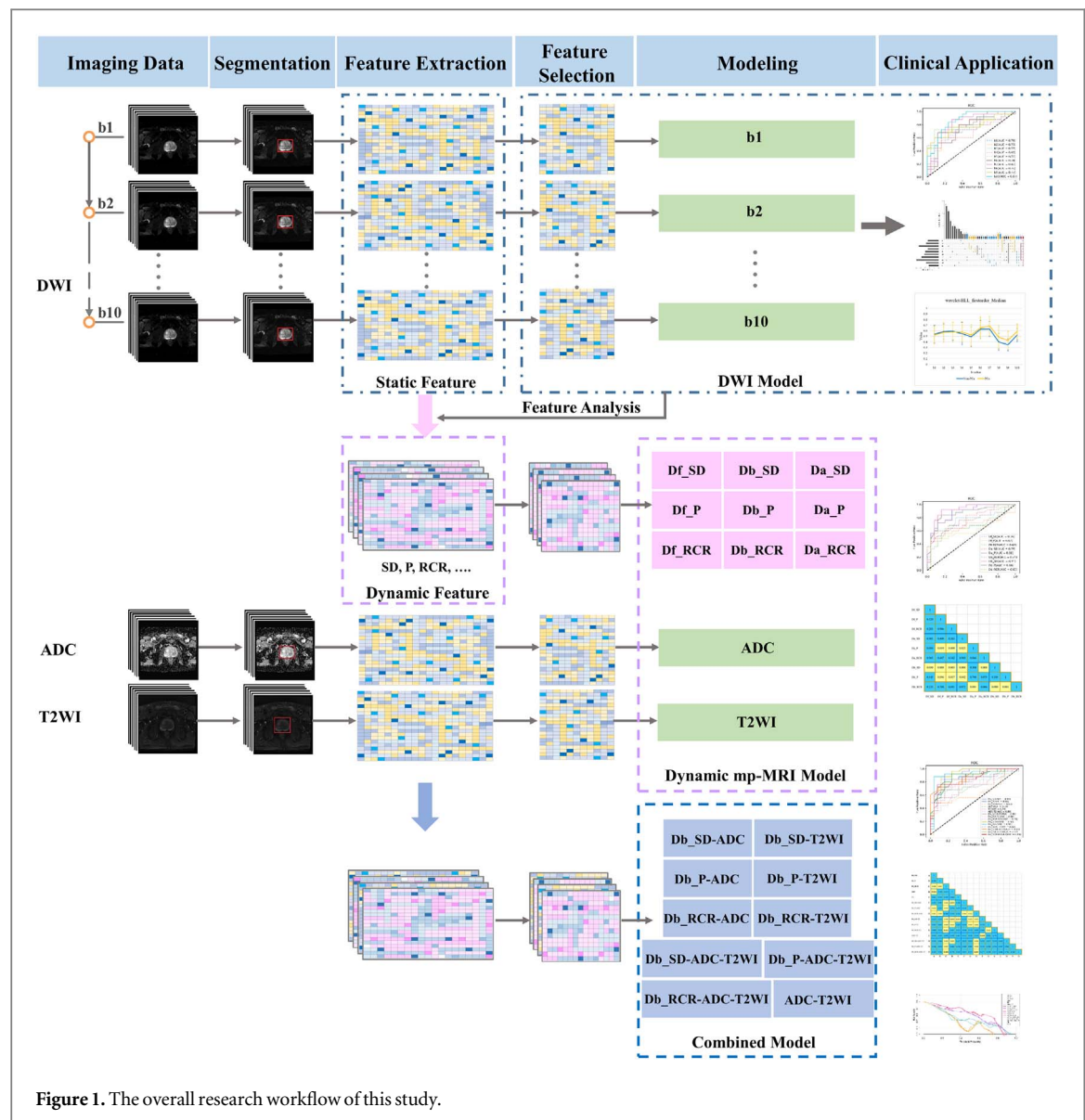
Figure 1. The overall research workflow of this study.

MRI parameters

All patients were examined on a 3.0T MRI system (SIGNA Pioneer, GE Healthcare, Milwaukee, USA). The mpMRI protocol included axial T1-weighted (T1w) fast spin echo (FSE), T2-weighted (T2w) FSE, spin-echo echo-planar imaging pulse IVIM-DWI, and DCE. This study focuses on axial T2w FSE and IVIM-DWI sequences at *b*-values of 10, 50, 100, 150, 200, 400, 600, 800, 1000, 1500 s mm^{-2}. The corresponding ADC maps were calculated automatically by the GE Healthcare workstation using IVIM-DWI (*b* values = 10, 1500 s mm^{-2}). For details about parameter settings, see table S1 in the supplementary A.

Figure 2 shows IVIM-DWI at different *b*-values, from which we can see that there are obvious differences in the images. In fact, the smaller the *b*-value is, the less sensitive it is to the detection of diffusion, and the more the image tends to reflect the microcirculatory perfusion of local tissues, but the signal of the whole image will be higher and the signal-to-noise ratio (SNR) is better. On the contrary, the higher the *b*-value is, the more sensitive it is to the detection of diffusion, and the more the image tends to reflect the diffusion movement of water molecules in the tissue, but the signal of the whole image is low and the SNR is poor (Iima and Le Bihan 2016). Specifically, in figures 2(k)–(t), due to the restricted diffusion of water molecules in the region of the tumor lesion, the signal in this region gradually increases with the increase of *b*-value, which is especially evident in the high *b*-value images (p)–(t). Nevertheless, the SNR of the whole image decreases.

Image segmentation, feature extraction and selection

3D-Slicer Software (Version 4.11) was used by a uro-Radiologist with 8 years of experience (reader 1) to perform layer-by-layer region of interest (ROI) segmentation of the whole prostate on T2WI, all b-value IVIM-DWI, and ADC map, respectively. That is, a total of 12 segmentations (1 for T2WI, 10 for IVIM-DWI, and 1 for ADC) for
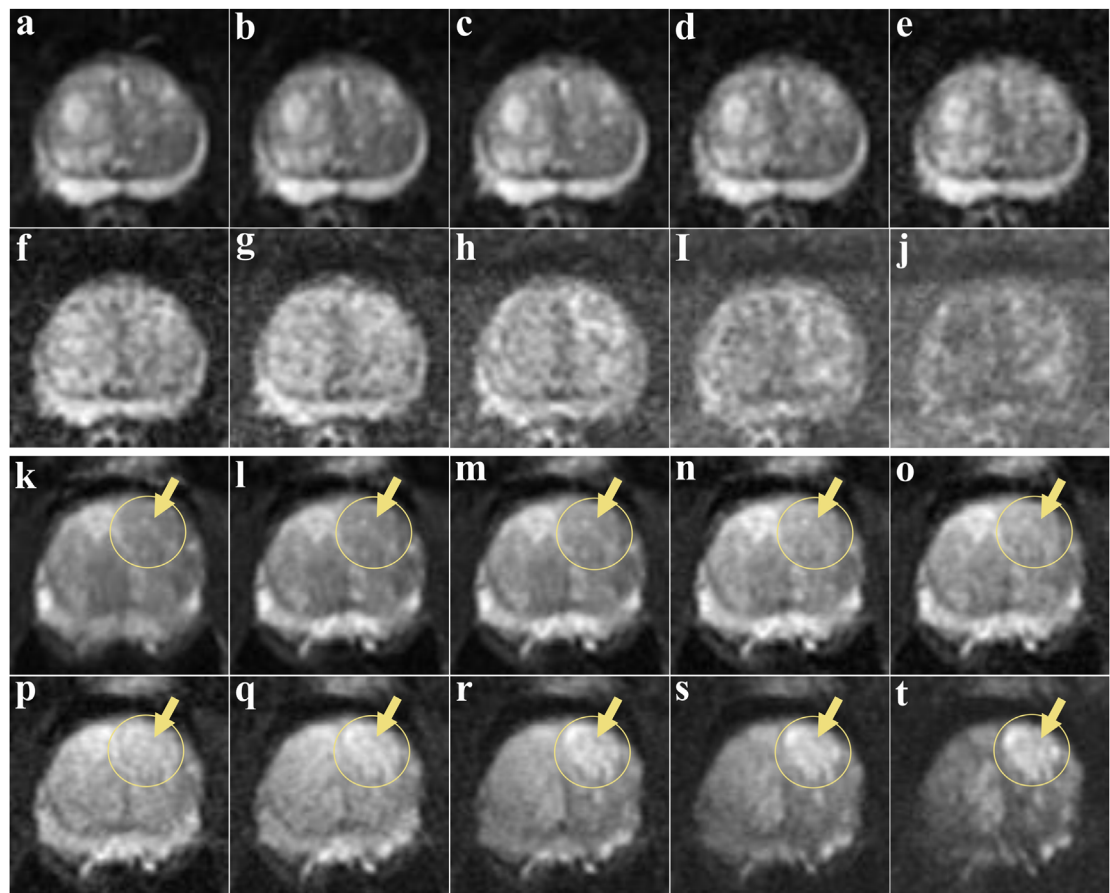
Figure 2. Intravoxel incoherent motion diffusion-weighted imaging (IVIM-DWI) at different *b*-values. Images (a)–(j) were obtained from a patient with benign prostate disease, and the corresponding *b*-values were 10, 50, 100, 150, 200, 400, 600, 800, 1000, 1500 s mm^{-2}, respectively. Images (k)–(t) were obtained from a patient with prostate cancer (PCa), and the corresponding b-values were 10, 50, 100, 150, 200, 400, 600, 800, 1000, 1500 s mm^{-2}, respectively.

each patient. The similarity/variation of segmentation was evaluated using Dice Similarity Coefficient (DSC) and Hausdorff Distance (HD), the results of which are shown in table S2 in the Supplementary Material.

The radiomics features of the segmented volume were extracted using the PyRadiomics package (van Griethuysen *et al* 2017) in Python (version 3.6). A total of 842 radiomics features were extracted from each ROI, including 106 original features and 736 wavelet features (Supplementary A).

To assess the reliability of image segmentation and the sensitivity of radiomics features to whole-gland segmentation, images of 30 patients randomly selected from the training cohort after 5 months were re-segmented independently by two uro-Radiologist with 8 (reader 1) and 10 (reader 2) years of experience, respectively. And intra- and interclass correlation coefficients (ICC) were computed to assess the intra- and interobserver reliability of image segmentation and radiomics features. Further details are described in the Supplementary A.

The least absolute shrinkage and selection operator (LASSO) (Tibshirani 1996) was used to select non-redundant and robust key features from the extracted radiomics features. The penalty parameter involved in this algorithm was related to the final number of selected features, which was tuned by ten-fold cross-validation in the training cohort.

The data processing for feature selection and modeling is shown in figure 3.

DWI model building

In order to (1) evaluate the predictive performance of DWI models constructed from key features of DWI with different *b*-values, (2) compare and analyze the similarities and differences of key feature types of DWI at different *b*-values, and (3) analyze the variations and differences of key features of DWI at different *b*-values, 10 IVIM-DWI sequences at different *b*-values were used to construct 10 DWI models: b1, b2, b3, b4, b5, b6, b7, b8, b9, b10. This step is the overall analysis of the variation difference of key DWI features at different *b*-values, which is the basis of dynamic features construction.

Figure 3. Flow diagram of the data processing for feature selection and modeling.
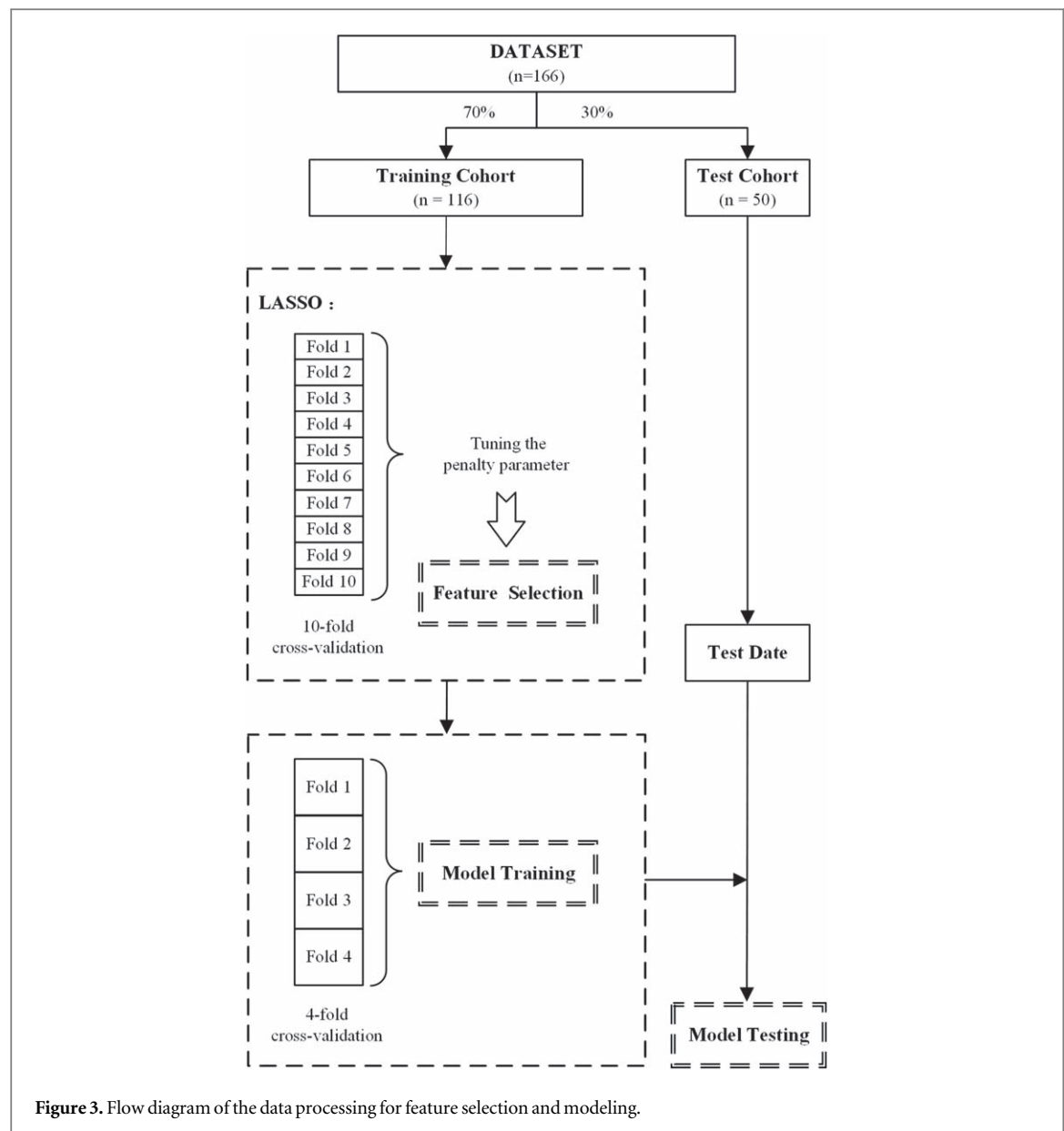
Dynamic features construction

We constructed the following three dynamic features to reflect the changes of traditional static radiomics features of DWI at different b-values.

(1) Standard discrete (SD) feature that reflects the mean deviation characteristics of static radiomics features at different b-values:

$$\mathrm{SD}(S(x(b))) = \frac{1}{k}\sum_{i=1}^{k}|S(x(bi)) - S(x(\overline{bi}))|, \quad 1 \leqslant i \leqslant k$$

(2) Relative change rate (RCR) feature that reflects the relative change rate characteristics of static radiomics features at every two different b-values:

$$\mathrm{RCR}(S(x(b))) = \frac{|S(x(bj)) - S(x(bi))|}{S(x(bi))}, \quad 1 \leqslant j < i \leqslant k$$

(3) Curve fitting parameter (P) feature that reflects change rule characteristics of static radiomics features at different b-values. In this study, we used a polynomial curve model to fit the values of static radiomics features for each b-value. The least square method is used to calculate the undetermined parameters, which

can be used as our dynamic features to represent the differences between these curve fitting models (Chen *et al* 2020):

$$
\begin{cases}
\hat{\theta} = \underset{\theta \in \Theta}{\arg\min} \sum_{i=0}^{k-1} (S(x(bi)) - m(bi, \theta))^2, \quad 1 \leqslant i \leqslant k \\[3mm]
m(bi, \theta) = \sum_{i=0}^{k-1} c_i b^i, \quad \theta = (c_0, c_1, \ldots, c_{k-1})^T
\end{cases},
$$

where $x(b)$ represents the region of interest extracted from medical images at diffusion gradient factor b; S function represents the traditional static radiomics features extraction method; $D(S(x(b)))$ represents the transformation from $\mathbb{R}^k$ to $\mathbb{R}^d$, that is, from static features to dynamic features. k is the number of DWI sequences at different b-values studied (k is 5, 5, 10 respectively in this study), and d is the number of dynamic features species that can be extracted; $\hat{\theta}$ is the dynamic feature P based on the least square estimation model; Θ represents a matrix.

In this study, IVIM-DWI of b1–b5, b6–b10, b1–b10 (b-values of b1–b10 are 10, 50, 100, 150, 200, 400, 600, 800, 1000, 1500 s mm^{-2} respectively.) were respectively used to construct the following three groups of dynamic features: (1) Df_SD, Df_P, Df_RCR; (2) Db_SD, Db_P, Db_RCR; (3) Da_SD Da_P, Da_RCR. Where, 'D' stands for dynamic features, 'f', 'b', and 'a' represent the b-values were taken the front part (b1–b5), the back part (b6–b10), and all (b1–b10) of the b-values set, respectively.

Dynamic mpMRI model and combined model construction

We constructed dynamic mpMRI models based on different key dynamic features of DWI, ADC and T2WI. Furthermore, in order to expore the prediction performance of combined sequences in mpMRI, we combined dynamic DWI (based on key dynamic features), ADC and T2WI single-sequence radiomics models respectively to construct 10 combined models: Db_SD + ADC, Db_P + ADC, Db_RCR + ADC, Db_SD + T2WI, Db_P + T2WI, Db_RCR + T2WI, ADC + T2WI, Db_SD + ADC + T2WI, Db_P + ADC + T2WI, Db_RCR + ADC + T2WI.

In our study, three machine learning methods were successively used for all prediction modeling: Support Vector Machine (SVM), Random Forests (RF) and Linear Discriminant Analysis (LDA). All three methods were implemented in Python using the Scikit-learn toolbox (http://scikit-learn.org/). Among them, SVM with radial basis functions (RBF) used the GridSearchCV function in Scikit-learn to conduct grid search to determine the optimal hyperparameters. RF was built from 200 trees, and the random_state parameter was set to 20 for reproducibility. All models were trained with 100 repetitions of four-fold cross-validation in the training cohort and validated in the independent test cohort.

Statistical analyses

In this study, the normal distribution of the experimental cohort could not be accurately judged due to its small number, so a non-parametric test with two independent samples was used. A Mann–Whitney U test was used to evaluate the difference between the training cohort and the test cohort in statistics software MedCalc (Version 20.023).

The performance of each prediction model was evaluated using sensitivity, specificity, positive predictive value (PPV), negative predictive value (NPV), accuracy, and area under the curve (AUC), and calculated using the Scikit-learn toolbox in Python. In MedCalc, DeLong test was used to compare whether the differences in AUC of each model were statistically significant. The Decision curve analysis (DCA) (Vickers and Elkin 2006) demonstrates net benefits (NB) at a range of threshold probabilities related to clinical outcomes. The NB combines the benefit of intervening (e.g. performing a needle biopsy) for correctly classified patients with the loss of intervening for incorrectly classified patients. We used DCA in R statistical software (Version 4.1.1) to calculate the net benefits generated by different models and evaluate their clinical utility.

For all tests, a two-sided $p < 0.05$ was considered statistically significant.

Results

Patient characteristics and radiomics features

The clinical and demographic data of 166 patients are reported in table 1. Among 116 training cohort, there were 57 and 59 patients with PCa and benign prostate disease, respectively. There were 25 PCa and 25 benign prostate disease patients in 50 test cohort. No significant difference was found in age and PSA, malignant versus benign ratio and Gleason score distribution between the training cohort and test cohort ($p = 0.487$ and $p = 0.127$, respectively).
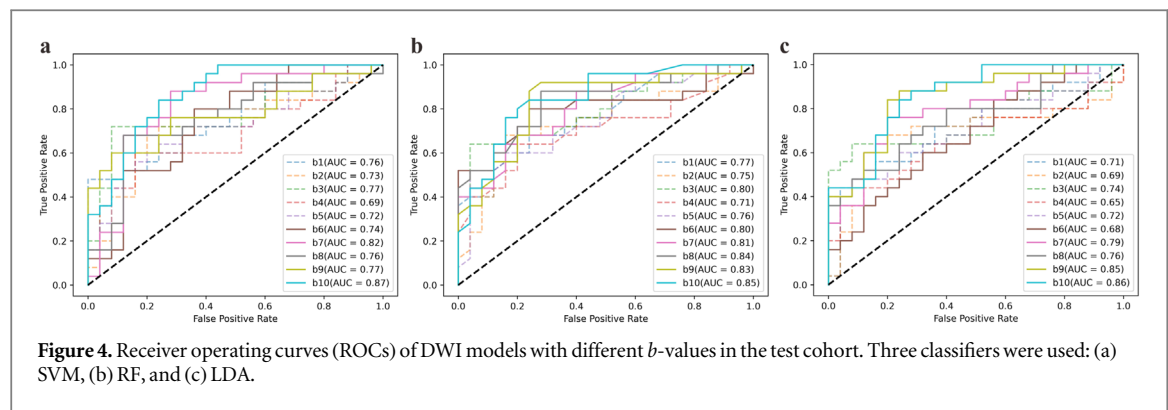
Figure 4. Receiver operating curves (ROCs) of DWI models with different *b*-values in the test cohort. Three classifiers were used: (a) SVM, (b) RF, and (c) LDA.

Table 1. Patient population clinical and demographic characteristics.

Characteristics	Total	Training cohort	Test cohort	*P*-value
Number, *n* (%)	166(100)	116(69.88)	50(30.12)	—
Age, median (IQR), years	66(60, 73)	66(60, 73)	67(61, 73)	0.4867[a]
PSA, median (IQR), ng ml^{-1}	11.80(7.78, 22.73)	12.10(8.69, 23.90)	10.38(7.12, 18.00)	0.1268 [a]
Non-PCa, *n* (%)	84(50.6)	59(50.9)	25(50)	0.9191[a]
PCa, *n* (%)	82(49.4)	57(49.1)	25(50)	
		Gleason score (biopsy), *n* (%)		0.0574[a]
6	13(15.9)	6(10.5)	7(28.0)	—
7	27(32.9)	18(31.6)	9(36.0)	—
8	12(14.6)	9(15.8)	3(12.0)	—
9	18(22.0)	15(26.3)	3(12.0)	—
10	12(14.6)	9(15.8)	3(12.0)	—

The *p*-values are presented for an intergroup comparison between the training cohort and test cohort performed using the Mann–Whitney U test.

[a] No difference was found between the training and test cohorts. IQR = interquartile range; PSA = prostate-specific antigen; PCa = prostate cancer.

For each image sequence, the intra- and interobserver ICC calculated based on two observers' segmentation data were greater than 0.75 (table S3 of the supplementary A). Therefore, the segmentation and radiomics features in this study had good reliability.

Key radiomics features selected for the three models are summarized in tables S4, S6 and S7 respectively in supplementary materials.

Predictive performance of DWI model and static features analysis

Table 2 shows the predictive performance of DWI models with different *b*-values using three machine learning methods in the test cohort, and their receiver operating curves (ROCs) are given in figure 4. For the three classifiers, the classification performance of DWI at different *b*-values was different, and the prediction performance of DWI models with the last five higher *b*-values was generally better than that of DWI models with the first five lower *b*-values.

The static key features used to identify PCa in DWI had significantly different intersections between high and low *b*-values (figure S1 of the supplementary B). Furthermore, the values of some static key features of DWI changed with the increase of *b*-values. Under the conditions of the last five high *b*-values, due to the significant difference of *b*-values, the feature values changed greatly (figure S2 of the supplementary B).

Predictive performance of dynamic mpMRI model and combined model

Because the overall results of RF classifier were slightly better than SVM and LDA classifiers in the predictive performance of all models, we only summarized and discussed the results of using RF classifier in the following. In addition, predictive performance of the dynamic mpMRI model and combined model based on SVM/LDA classifier are presented in tables S8 and S9 in the supplementary material.

Among the three groups of dynamic features, in general, the dynamic features constructed based on the static features of IVIM-DWI at b6–b10 had the best detection performance for PCa (table 3, figure 5(a)). Db_SD performed best, with sensitivity, specificity, PPV, NPV, accuracy and AUC of 82.56%, 82.76%, 82.87%, 82.90%,

Table 2. Predictive performance of DWI models with different *b*-values using three machine learning methods in the test cohort.

Model (NKF)		Sensitivity (%)	Specificity (%)	PPV (%)	NPV (%)	Accuracy (%)	AUC (%)
SVM	b1 (11)	57.44 ± 5.81	74.24 ± 6.60	69.54 ± 5.01	63.66 ± 2.31	65.84 ± 2.43	75.86 ± 1.15
	b2 (13)	70.56 ± 3.86	70.40 ± 5.66	70.68 ± 3.82	70.56 ± 2.52	70.48 ± 2.69	72.72 ± 2.50
	b3 (21)	69.28 ± 4.66	77.56 ± 7.69	76.05 ± 6.17	71.65 ± 3.28	73.42 ± 3.98	76.66 ± 3.08
	b4 (11)	60.40 ± 2.86	63.52 ± 8.30	62.81 ± 5.50	61.41 ± 3.14	61.96 ± 4.06	68.65 ± 3.14
	b5 (14)	61.80 ± 5.97	67.48 ± 12.44	66.78 ± 7.92	63.66 ± 3.35	64.64 ± 4.78	71.96 ± 3.71
	b6 (15)	61.08 ± 9.91	72.72 ± 9.69	69.81 ± 7.00	65.53 ± 5.79	66.90 ± 5.28	**74.38 ± 4.66**
	b7 (18)	67.52 ± 6.18	77.04 ± 6.76	74.97 ± 5.75	70.48 ± 4.16	72.28 ± 4.23	**81.93 ± 3.25**
	b8 (25)	70.20 ± 4.88	72.20 ± 8.24	72.14 ± 5.74	70.81 ± 3.36	71.20 ± 3.97	**76.10 ± 3.56**
	b9 (13)	62.80 ± 7.10	78.40 ± 7.69	74.83 ± 6.70	67.93 ± 4.66	70.60 ± 5.11	**77.23 ± 5.20**
	b10 (10)	53.44 ± 7.66	87.12 ± 3.08	80.67 ± 3.40	65.39 ± 3.52	70.28 ± 3.32	**86.82 ± 1.51**
RF	b1 (11)	63.96 ± 6.05	71.68 ± 7.75	69.79 ± 5.34	66.65 ± 3.27	67.82 ± 3.53	76.77 ± 2.35
	b2 (13)	68.80 ± 2.99	72.52 ± 6.52	71.80 ± 4.93	69.88 ± 2.46	70.66 ± 3.24	74.55 ± 2.74
	b3 (21)	66.00 ± 4.25	83.28 ± 7.51	80.52 ± 6.61	71.03 ± 2.25	74.64 ± 3.21	80.29 ± 2.97
	b4 (11)	62.96 ± 3.56	73.04 ± 6.56	70.38 ± 4.64	66.32 ± 2.35	68.00 ± 3.03	70.88 ± 1.94
	b5 (14)	64.24 ± 5.39	69.28 ± 8.39	68.15 ± 5.52	65.95 ± 3.44	66.76 ± 3.98	75.52 ± 2.57
	b6 (15)	67.72 ± 7.97	80.28 ± 10.36	78.53 ± 7.70	71.58 ± 4.51	74.00 ± 4.69	**79.72 ± 3.36**
	b7 (18)	64.60 ± 9.00	78.32 ± 8.80	75.48 ± 7.32	69.22 ± 5.71	71.46 ± 5.40	**81.40 ± 3.76**
	b8 (25)	73.08 ± 9.70	77.12 ± 7.20	76.50 ± 5.09	74.79 ± 6.41	75.10 ± 4.62	**83.46 ± 3.23**
	b9 (13)	71.52 ± 7.93	78.20 ± 4.36	76.70 ± 3.60	73.70 ± 5.29	74.86 ± 3.97	**83.28 ± 2.28**
	b10 (10)	70.96 ± 7.93	82.84 ± 3.36	80.56 ± 2.94	74.42 ± 4.92	76.90 ± 3.71	**85.32 ± 2.19**
LDA	b1 (11)	58.96 ± 6.83	72.16 ± 5.63	68.05 ± 4.64	63.92 ± 4.08	65.56 ± 3.97	71.18 ± 2.46
	b2 (13)	70.24 ± 3.55	71.04 ± 7.22	71.15 ± 5.45	70.41 ± 3.23	70.64 ± 4.03	68.58 ± 2.27
	b3 (21)	64.28 ± 4.91	75.32 ± 8.20	72.84 ± 6.94	67.80 ± 3.75	69.80 ± 4.60	74.43 ± 3.80
	b4 (11)	58.84 ± 3.45	67.52 ± 6.41	64.71 ± 4.62	62.06 ± 2.84	63.18 ± 3.47	65.32 ± 2.03
	b5 (14)	62.04 ± 6.08	64.84 ± 9.44	64.45 ± 6.24	63.07 ± 3.90	63.44 ± 4.36	71.56 ± 3.91
	b6 (15)	53.28 ± 4.45	67.92 ± 7.33	62.86 ± 5.68	59.19 ± 3.00	60.60 ± 3.78	**67.77 ± 3.60**
	b7 (18)	62.20 ± 5.07	82.76 ± 4.41	78.44 ± 4.37	68.73 ± 3.10	72.48 ± 3.32	**79.40 ± 2.99**
	b8 (25)	67.04 ± 4.20	73.88 ± 7.65	72.41 ± 5.78	69.11 ± 3.25	70.46 ± 4.05	**75.63 ± 1.81**
	b9 (13)	79.16 ± 4.36	79.84 ± 4.08	79.82 ± 3.14	79.44 ± 3.33	79.50 ± 2.58	**84.86 ± 1.63**
	b10 (10)	66.52 ± 7.26	83.96 ± 4.02	80.67 ± 3.74	71.76 ± 4.22	75.24 ± 3.59	**86.04 ± 2.12**

The AUC values of DWI models with the last five higher b-values are highlighted in bold. All values in the table are expressed with mean ± standard deviation (SD). NKF = the number of key features; NPV = negative predictive value; PPV = positive predictive value; AUC = area under the receiver operator characteristic curve; SVM = Support Vector Machine; RF = Random Forests; LDA = Linear Discriminant Analysis; b1–b10 = DWI models with b-values of 10, 50, 100, 150, 200, 400, 600, 800, 1000 and 1500 s mm^{-2} respectively.

82.66% and 90.78%, respectively. In contrast, Db_RCR performed poorly, with sensitivity, specificity, PPV, NPV, accuracy and AUC of 59.60%, 60.40%, 60.41%, 60.07%, 60.00% and 63.02%, respectively.
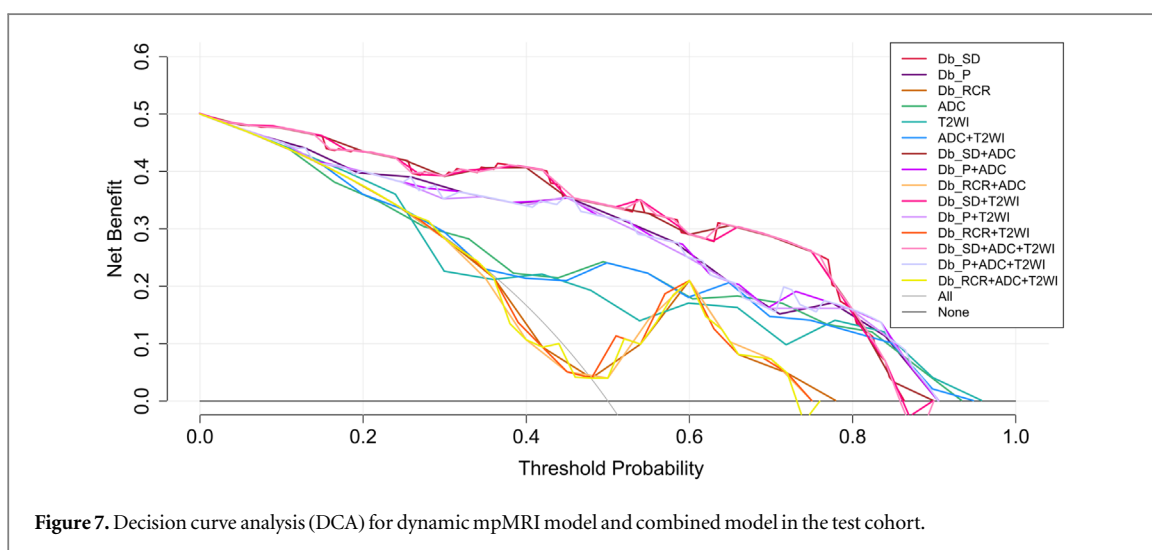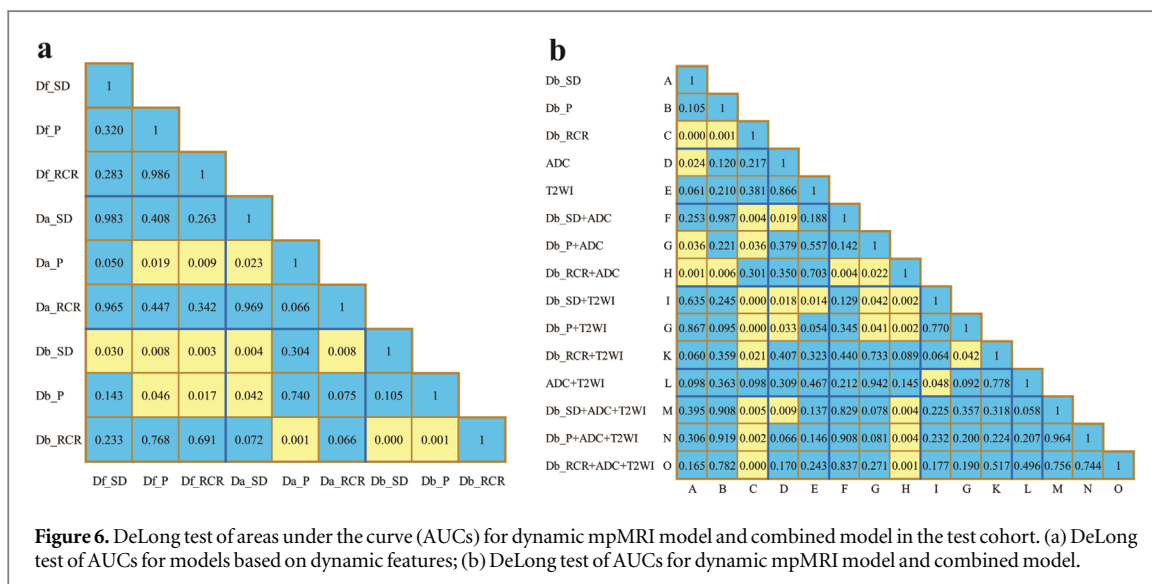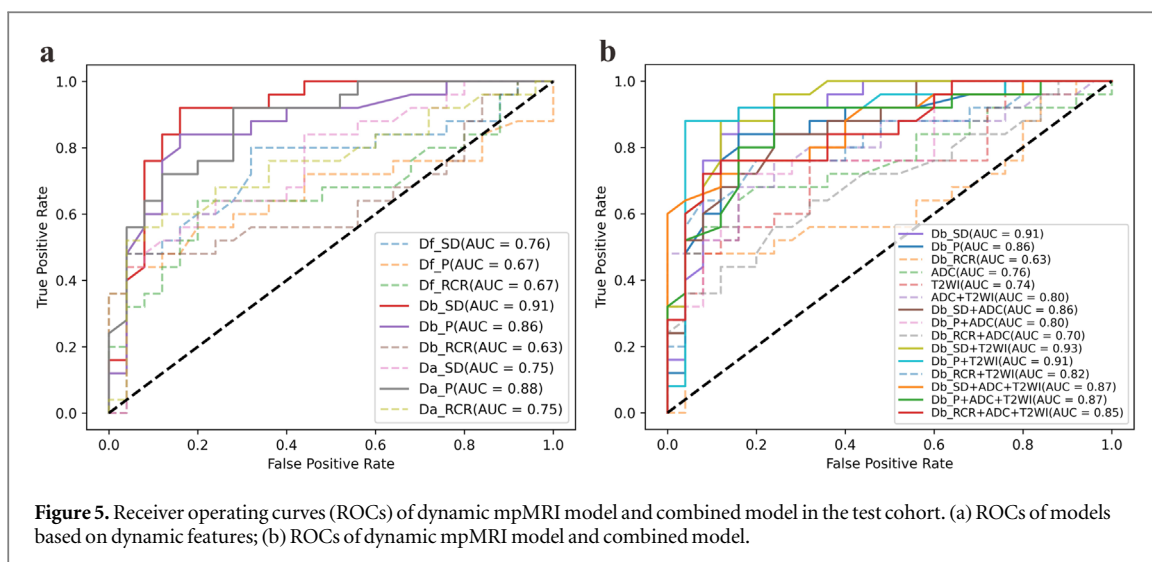
In the dynamic mpMRI model and combined model, in general, the combined model with static features of T2WI and dynamic features had the best prediction effect on PCa (table 3, figure 5(b)). The AUC of Db_SD + T2WI, Db_P + T2WI, and Db_RCR + T2WI were 92.90%, 91.29%, and 81.46%, respectively. Db_SD + T2WI showed the best performance, with sensitivity, specificity, PPV, NPV, accuracy and AUC of 79.76%, 89.04%, 88.25%, 81.87%, 84.40% and 92.90%, respectively. The predictive performance of Db_SD + T2WI was significantly improved compared with T2WI (AUC of T2WI was 73.87%, $p = 0.014$). Compared with the Db_RCR, the prediction performance of Db_RCR + T2WI was improved considerably (AUC of Db_RCR was 63.02%, AUC of Db_RCR + T2WI was 81.46%, $p = 0.021$). However, the combination of static features of the two modal images (ADC + T2WI) did not significantly improve the prediction performance of the model ($p = 0.309$, $p = 0.467$). In the combination model composed of two modal images, the addition of ADC static features failed to improve the identification performance of dynamic features for PCa. Furthermore, the prediction performance of the combined model composed of three modal images was not significantly improved compared with that of the two models. In addition, the performance of Db_SD was significantly better than that of ADC commonly used in most studies (AUC of Db_SD was 90.78%, AUC of ADC is 75.48%, $p = 0.024$). Figure 6 shows the comparison results of AUCs of all models in the test cohort using the DeLong test.

DCA for dynamic mpMRI and combined model in the test cohort is presented in figure 7. When the threshold probability is 0–0.8, the model based on dynamic feature Db_SD had the largest net benefit for patients, that is, they had the highest clinical application value for patients. This will help doctors personalize treatment for patients, thereby avoiding some unnecessary needle biopsies and reducing the risk of side effects.

Table 3. Predictive performance of the dynamic MpMRI model and combined model using random forests (RF) classifier.

Model (NKF)		Sensitivity (%)	Specificity (%)	PPV (%)	NPV (%)	Accuracy (%)	AUC (%)
Dynamic	Df_SD (8)	68.68 ± 6.91	69.24 ± 6.34	69.26 ± 4.32	69.10 ± 4.46	68.96 ± 3.87	75.52 ± 2.58
mpMRI	Df_P (2)	56.84 ± 6.41	66.28 ± 10.80	63.63 ± 7.39	60.44 ± 4.07	61.56 ± 4.96	66.83 ± 3.25
Model	Df_RCR (34)	52.60 ± 7.12	75.76 ± 8.12	69.13 ± 6.35	61.59 ± 3.01	64.18 ± 3.70	66.77 ± 2.64
	Db_SD (18)	82.56 ± 5.89	82.76 ± 3.99	82.87 ± 3.04	82.90 ± 4.34	82.66 ± 2.71	**90.78 ± 1.59**
	Db_P (14)	68.04 ± 6.96	87.52 ± 5.10	84.84 ± 4.93	73.49 ± 3.94	77.78 ± 3.47	**86.35 ± 2.08**
	Db_RCR (16)	59.60 ± 7.83	60.40 ± 8.66	60.41 ± 4.14	60.07 ± 3.45	60.00 ± 3.36	63.02 ± 2.55
	Da_SD (18)	63.24 ± 6.21	71.48 ± 7.19	69.24 ± 5.67	66.14 ± 4.05	67.36 ± 4.29	75.39 ± 3.08
	Da_P (10)	70.60 ± 5.81	86.00 ± 5.75	83.84 ± 4.89	74.71 ± 3.51	78.30 ± 3.13	**87.60 ± 2.55**
	Da_RCR (38)	59.60 ± 6.75	81.56 ± 7.18	77.04 ± 5.83	67.02 ± 3.07	70.58 ± 3.28	75.09 ± 2.48
	ADC (19)	65.24 ± 4.92	81.68 ± 5.52	78.36 ± 4.79	70.21 ± 3.06	73.46 ± 3.38	75.48 ± 2.16
	T2WI (37)	58.48 ± 8.46	75.44 ± 9.45	71.24 ± 7.99	64.66 ± 4.51	66.96 ± 5.16	73.87 ± 4.20
Combined	Db_SD + ADC (22)	72.32 ± 7.15	81.20 ± 5.08	79.60 ± 3.98	74.92 ± 4.49	76.76 ± 3.30	86.09 ± 2.08
Model	Db_P + ADC (26)	63.52 ± 6.02	81.76 ± 4.74	77.86 ± 4.68	69.29 ± 3.61	72.64 ± 3.59	79.37 ± 2.57
	Db_RCR + ADC (36)	58.16 ± 6.94	67.68 ± 10.02	64.96 ± 6.31	61.77 ± 4.14	62.92 ± 4.62	69.67 ± 2.96
	Db_SD + T2WI (39)	79.76 ± 6.90	89.04 ± 4.44	88.25 ± 3.64	81.87 ± 4.61	84.40 ± 2.62	**92.90 ± 2.05**
	Db_P + T2WI (18)	82.72 ± 4.41	88.32 ± 4.37	87.86 ± 3.91	83.81 ± 3.21	85.52 ± 2.32	**91.29 ± 1.66**
	Db_RCR + T2WI (39)	67.68 ± 8.61	80.96 ± 6.43	78.44 ± 5.15	71.89 ± 4.84	74.32 ± 3.93	**81.46 ± 3.61**
	ADC + T2WI (38)	64.40 ± 6.31	81.12 ± 6.74	77.77 ± 6.20	69.63 ± 3.93	72.76 ± 4.14	80.06 ± 3.81
	Db_SD + ADC + T2WI (43)	71.36 ± 6.81	86.80 ± 4.95	84.62 ± 4.87	75.42 ± 4.31	79.08 ± 3.88	86.83 ± 2.80
	Db_P + ADC + T2WI (27)	73.60 ± 5.77	83.52 ± 5.04	81.95 ± 4.43	76.15 ± 3.79	78.56 ± 3.37	86.78 ± 3.06
	Db_RCR + ADC + T2WI (26)	68.24 ± 7.52	83.52 ± 8.30	81.44 ± 6.37	72.77 ± 3.76	75.88 ± 3.31	85.08 ± 2.79

The bold number indicates models with better AUC results in the dynamic mpMRI model or combined model. All values in the table are expressed with mean ± standard deviation (SD). NKF = the number of key features; NPV = negative predictive value; PPV = positive predictive value; AUC = area under the receiver operator characteristic curve; 'Df_', 'Db_' and 'Da_' = the dynamic feature models are constructed from the static features of DWI at b-values of b1–b5, b6–b10 and b1–b10 respectively; ADC = the model of apparent diffusion coefficient; T2WI = the model of T2-weighted imaging.

Figure 5. Receiver operating curves (ROCs) of dynamic mpMRI model and combined model in the test cohort. (a) ROCs of models based on dynamic features; (b) ROCs of dynamic mpMRI model and combined model.

Figure 6. DeLong test of areas under the curve (AUCs) for dynamic mpMRI model and combined model in the test cohort. (a) DeLong test of AUCs for models based on dynamic features; (b) DeLong test of AUCs for dynamic mpMRI model and combined model.

Figure 7. Decision curve analysis (DCA) for dynamic mpMRI model and combined model in the test cohort.

Discussion

In our study, by analyzing the static radiomics features of IVIM-DWI sequences at different b-values, we constructed dynamic features that can reflect the comprehensive characteristics of multiple b-values DWI images. Through the construction of dynamic features, the transformation from static analysis to dynamic analysis of the prostate image was realized, which provided a way to obtain the feature change information that cannot be observed in PCa traditional static radiomics features analysis, so as to obtain more comprehensive prostate image information. Moreover, based on dynamic features, the dynamic mpMRI model and the combined model containing dynamic and static information had good PCa prediction effects in all the machine learning methods we used.

Previous studies on DWI radiomics of the prostate were only based on static radiomics features under specific *b*-value conditions (Cuocolo *et al* 2021, Leech *et al* 2021, Yi *et al* 2022). However, dynamic features can contribute to the accurate discrimination of the model by combining the variation difference and all-around performance of static radiomics features at different *b*-values. For example, original_glszm_LargeAreaHighGrayLevelEmphasis (the change of its value at different *b*-values is shown in figure S3 of the supplementary C) is a key feature of the Db_SD and Db_P model, at the same time also is the key feature of models b9, b10. In the b6–b10 condition, the feature values of non-PCa patients gradually increased and the slope increased, while the feature values of PCa patients were relatively stable.

In our research results, the diagnostic performance of dynamic feature models Db_SD and Db_P is better than that of traditional static feature models ADC and T2WI. This may be because dynamic feature models based on static feature changes in the overall situation may reduce the impact of individual non-specific performance on diagnostic results during image diagnosis. Furthermore, the combined model based on dynamic and T2WI static features performed best in our study, because these models combined the dynamic information of functional sequence DWI (Bihan *et al* 1988, Turkbey *et al* 2010) and the static information of T2WI sequence (Turkbey *et al* 2010) which can reflect the anatomical structure of the prostate. However, the addition of the ADC map did not play a similar role as the T2WI sequence, mainly for two reasons. On the one hand, the feature representation of ADC map is not as strong as that of Db_SD, so its addition did not improve the Db_SD model (AUC of Db_SD was 90.79%, AUC of Db_SD + ADC was 86.09%, $p = 0.253$). On the other hand, due to the small dataset of this study, overfitting of the model may occur. On the contrary, the ADC model was significantly improved by the addition of dynamic features of Db_SD (AUC of ADC was 75.48%, AUC of Db_SD + ADC was 86.09%, $p = 0.019$).

To our knowledge, this is the first study to propose a dynamic-static combination model based on the dynamic mpMRI radiomics method. However, previous radiomics combined models are based on static features of different modal images. (Zhang *et al* 2021a) demonstrated that combined mpMRI radiomics and clinical features can noninvasively predict microvascular invasion in patients with hepatocellular carcinoma. Romeo *et al* (2022) proved that the radiomics integrated model based on AI-enhanced simultaneous multiparametric ^{18}F-FDG PET/MRI can accurately distinguish benign and malignant breast lesions.

Our study found that dynamic features based on the last five high b-values have better performance in PCa identification than dynamic features based on the first five and all *b*-values. This may be because the static model of the last five high *b*-values have a slightly better prediction ability, and their *b*-values intensity varies greatly, resulting in a significant difference in the diffusion of water molecules, thus making the dynamic features contain more useful information for PCa discrimination. At the same time, it also indicates that PCa detection based on dynamic features is not simply the more *b*-values, the better; Instead, multiple high *b*-value images with potential in imaging diagnosis should be included, and the information reflected by them should be integrated to construct dynamic features, so as to assist the improvement of PCa detection ability.

In addition, manual segmentation of the whole prostate gland was adopted. Previous studies have tended to be based on tumor analysis (Bonekamp *et al* 2018, Cuocolo *et al* 2019, Bernatz *et al* 2020, Cuocolo *et al* 2021, Hectors *et al* 2021, Leech *et al* 2021, Sushentsev *et al* 2022, Yi *et al* 2022), but recent studies have also looked at the whole prostate gland, including the tumor and its surrounding environment. Gugliandolo *et al* (2021) based on the segmentation of the whole gland, constructing a radiomics model that combined oncological and radiological scores to classify PCa aggressiveness. Rodrigues *et al* (2021) demonstrated that models trained using the whole-gland radiomics features performed better than lesion volume of interest (VOI) radiomics features in identifying clinically significant PCa, and that the area surrounding the tumor lesion provided information related to Gleason score. There are two main reasons why we adopt the whole prostate gland segmentation method. On the one hand, whole gland segmentation is easier to achieve, and its feature extraction is robust (Rodrigues *et al* 2021). This is also reflected in our reliability assessment experiment on image segmentation and radiomics features. In addition, PCa is usually multifocal, and the use of multiple VOI means complex segmentation and radiomics related work. On the other hand, a large number of studies have shown that the surrounding environment of tumors plays an important role in their occurrence and growth (Dieterich and

Bikfalvi 2019, Sofopoulos *et al* 2019, Lugano *et al* 2020), and the perilesional radiomics features may contribute to the diagnosis of PCa (Gugliandolo *et al* 2021, Rodrigues *et al* 2021, Zhang *et al* 2021b).

Our study has several limitations. First, our dataset was relatively small, especially the number of insignificant PCa samples (Gleason score ≤6). Therefore, we only carried out a radiomics study on PCa benign and malignant differentiation, and did not carry out more clinically significant studies such as detection of significant PCa. In addition, this study was a single-center study, which needs to be further validated in a larger population with sufficient data. Second, the prostate biopsy results were used as the classification standard of PCa in our study, which may have sampling errors. Third, although the whole prostate gland improved the efficiency of the entire workflow and made good PCa prediction, it can still be further optimized by achieving precise automatic segmentation.

Conclusion

In conclusion, the dynamic mpMRI radiomics method has the potential to extract dynamic information and has good PCa detection ability. This method fully mined the PCa information contained in prostate images. Therefore, the dynamic-static combination model developed based on this method can improve the accuracy of PCa image diagnosis by comprehensively analyzing dynamic and traditional static radiomics features. Furthermore, the dynamic mpMRI radiomics method improves the application value of prostate imaging, thus providing doctors with a potential and quantitative method for PCa imaging diagnosis.

Funding

Informed consent

Patient consent was waived due to the retrospective design of the study.

Ethical approval

Institutional Review Board approval was obtained.

This clinical study was approved by the Ethics Committee of the First Hospital of China Medical University and was carried out in accordance with the Declaration of Helsinki (approval number: AF-SOP-07-1.1-01).

References

Ahmed H U *et al* 2017 Diagnostic accuracy of multi-parametric MRI and TRUS biopsy in prostate cancer (PROMIS): a paired validating confirmatory study *Lancet* **389** 815–22

Bernatz S *et al* 2020 Comparison of machine learning algorithms to predict clinically significant prostate cancer of the peripheral zone with multiparametric MRI using clinical assessment categories and radiomic features *Eur. Radiol.* **30** 6757–69

Bihan D L, Breton E, Lallemand D, Aubin M L, Vignaud J and Laval-Jeantet M 1988 Separation of diffusion and perfusion in intravoxel incoherent motion MR imaging *Radiology* **168** 497–505

Bonekamp D *et al* 2018 Radiomic machine learning for characterization of prostate lesions with MRI: comparison to ADC values *Radiology* **289** 128–37

Chen Y *et al* 2020 A new role of ^{11}C-Choline Pet in localizing the epileptogenic foci in insular cortex in the patients *CNS Neurosci. Ther.* **26** 144–7

Cuocolo R *et al* 2019 Clinically significant prostate cancer detection on MRI: a radiomic shape features study *Eur. J. Radiol.* **116** 144–9

Cuocolo R *et al* 2021 MRI index lesion radiomics and machine learning for detection of extraprostatic extension of disease: a multicenter study *Eur. Radiol.* **31** 7575–83

Dieterich L C and Bikfalvi A 2019 The tumor organismal environment: role in tumor development and cancer immunotherapy *Semin. Cancer Biol.* **65** 197–206

Fave X *et al* 2017 Delta-radiomics features for the prediction of patient outcomes in non-small cell lung cancer *Sci. Rep.* **7** 588

Fulgham P F *et al* 2017 AUA policy statement on the use of multiparametric magnetic resonance imaging in the diagnosis, staging and management of prostate cancer *J. Urol.* **198** 832–8

Gugliandolo S G *et al* 2021 MRI-based radiomics signature for localized prostate cancer: a new clinical tool for cancer aggressiveness prediction ? Sub-study of prospective phase II trial on ultra-hypofractionated radiotherapy (AIRC IG-13218) *Eur. Radiol.* **31** 716–28

Hectors S J *et al* 2021 Magnetic resonance imaging radiomics-based machine learning prediction of clinically significant prostate cancer in equivocal PI-RADS 3 lesions *J. Magn. Reson. Imaging* **54** 1466–73

Hofbauer S L *et al* 2018 Validation of prostate imaging reporting and data 9. System version 2 for the detection of prostate cancer *J. Urol.* **200** 767–73

Iima M and Le Bihan D 2016 Clinical intravoxel incoherent motion and diffusion MR imaging: past, present, and future *Radiology* **278** 13–32

Kasivisvanathan V *et al* 2018 MRI-targeted or standard biopsy for prostate-cancer diagnosis *New Engl. J. Med.* **378** 1767–77

Kooreman E S *et al* 2021 Daily intravoxel incoherent motion (IVIM) In Prostate Cancer patients during MR-guided radiotherapy-a multicenter study *Front. Oncol.* **11** 705964

Lambin P *et al* 2012 Radiomics: extracting more information from medical images using advanced feature analysis *Eur. J. Cancer* **48** 441–6

Leech M, Osman S, Jain S and Marignol L 2021 Mini review: personalization of the radiation therapy management of prostate cancer using MRI-based radiomics *Cancer Lett* **498** 210–6

Limkin E J *et al* 2017 Promises and challenges for the implementation of computational medical imaging (radiomics) in oncology *Ann. Oncol.* **28** 1191–206

Liu Z *et al* 2019 The applications of radiomics in precision diagnosis and treatment of oncology: opportunities and challenges *Theranostics* **9** 1303–22

Lugano R, Ramachandran M and Dimberg A 2020 Tumor angiogenesis: causes, consequences, challenges and opportunities *Cell. Mol. Life Sci.* **77** 1745–70

Mottet N *et al* 2022 EAU-EANM-ESTRO-ESUR-ISUP-SIOGGUIDELINES ON PROSTATE CANCER 2022 Available from:https:// d56bochluxqnz.cloudfront.net/documents/full-guideline/EAU-EANM-ESTRO-ESUR-ISUP_SIOG-Guidelines-on-Prostate-Cancer-2022_2022-04-25-063938_yfos.pdf

Qu H *et al* 2022 Dynamic radiomics: a new methodology to extract quantitative time-related features from tomographic images *Appl. Intell.* **52** 11827–45

Rodrigues A, Santinha J, Galvão B, Matos C, Couto F M and Papanikolaou N 2021 Prediction of prostate cancer disease aggressiveness using bi-parametric mri radiomics *Cancers* **13** 6065

Romeo V *et al* 2022 AI-enhanced simultaneous multiparametric ^{18}F-FDG PET/MRI for accurate breast cancer diagnosis *Eur. J. Nucl. Med. Mol. Imaging* **49** 596–608

Russo G, Mischi M, Scheepens W, Rosette J J D L and Wijkstra H 2012 Angiogenesis in prostate cancer: onset, progression and imaging *BJU Int.* **110** E794–808

Sauer M *et al* 2018 Preoperative evaluation of pelvine lymph node metastasis in high risk prostate cancer with intravoxel incoherent motion (IVIM) MRI *Eur. J. Radiol.* **107** 1–6

Sofopoulos M *et al* 2019 The prognostic significance of peritumoral tertiary lymphoid structures in breast cancer *Cancer Immunol. Immunother.* **68** 1733–45

Sung H *et al* 2021 Global cancer statistics 2020: GLOBOCAN estimates of incidence and mortality worldwide for 36 cancers in 185 countries *CA Cancer J. Clin.* **71** 209–49

Sushentsev N *et al* 2022 Comparative performance of MRI-derived PRECISE scores and delta-radiomics models for the prediction of prostate cancer progression in patients on active surveillance *Eur. Radiol.* **32** 680–9

Thompson J E *et al* 2016 The diagnostic performance of multiparametric magnetic resonance imaging to detect significant prostate cancer *J. Urol.* **195** 1428–35

Tibshirani R 1996 Regression shrinkage and selection via the lasso *J. R. Stat. Soc.* B **58** 267–88

Turkbey B *et al* 2010 Prostate cancer: value of multiparametric MR imaging at 3 T for detection—histopathologic correlation *Radiology* **255** 89–99

Turkbey B *et al* 2019 Prostate imaging reporting and data system version 2.1: 2019 update of Prostate Imaging Reporting and Data System Version 2 *Eur. Urol.* **0232** 1–12

van Griethuysen J J M *et al* 2017 Computational radiomics system to decode the radiographic phenotype *Cancer Res.* **77** e104–7

Vickers A J and Elkin E B 2006 Decision curve analysis: a novel method for evaluating prediction models *Med. Decis Mak* **26** 565–74

Weinreb J C *et al* 2016 PI-RADS Prostate Imaging—reporting and data system: 2015, Version 2 *Eur. Urol.* **69** 16–40

Yi Z *et al* 2022 Machine learning-based prediction of invisible intraprostatic prostate cancer lesions on ^{68}Ga-PSMA-11 PET/CT in patients with primary prostate cancer *Eur. J. Nucl. Med. Mol. Imaging* **49** 1523–34

Zhang H *et al* 2021b Diagnostic nomogram based on intralesional and perilesional radiomics features and clinical factors of clinically significant prostate cancer *J. Magn. Reson. Imaging* **53** 1550–8

Zhang Y *et al* 2021a Preoperative prediction of microvascular invasion in hepatocellular carcinoma via multi-parametric MRI radiomics *Front. Oncol.* **11** 633596